Probing the $NO_2 \to NO + O$ transition state via time resolved unimolecular decomposition

S. I. Ionov, G. A. Brucker,[a] C. Jaques, Y. Chen,[b] and C. Wittig
Department of Chemistry, University of Southern California, Los Angeles, California 90089-0482

Time resolved, subpicosecond resolution measurements of photoinitiated NO_2 unimolecular decomposition rates are reported for expansion cooled and room temperature samples. The molecules are excited by 375–402 nm tunable subpicosecond pulses having bandwidths $\geqslant 20$ cm^{-1} to levels which are known to be thorough admixtures of the $^2B_2$ electronically excited state and the $^2A_1$ ground electronic state. Subsequent decomposition is probed by a 226 nm subpicosecond pulse that excites laser-induced fluorescence (LIF) in the NO product. When increasing the amount of excitation over the dissociation threshold, an uneven, "step-like" increase of the decomposition rate vs energy is observed for expansion cooled samples. The steps are spaced by ~ 100 cm^{-1} and can be assigned *ad hoc* to bending at the transition state. Relying on experimental estimates for the near threshold density of states, we point out that simple transition state theory predictions give rates that are consistent with these measured values. The rates are sufficiently rapid to question the assumption of rapid intramolecular vibrational redistribution, which is implicit in transition state theories. In contrast to expansion cooled samples, room temperature samples exhibit a smooth variation of the reaction rate vs photon energy. By comparing rates for rotationally cold and room temperature NO_2, the ON–O bond is estimated to be $\sim 40\%$ longer in the transition state than in the parent molecule.

I. INTRODUCTION

When reaction rate theories such as Rice–Ramsperger–Kassel–Marcus (RRKM),[1,2] phase space theory (PST),[3,4] and the statistical adiabatic channel model (SACM)[5–7] were first introduced for the purpose of describing unimolecular decomposition, it was hoped that they could reconcile large bodies of data of varying degrees of experimental resolution. This worked for a while, but recent experimental advances have presented new challenges and stimulated new developments. Employing expansion cooling techniques and preparing reactive species by using tunable, narrow bandwidth laser radiation, virtually monoenergetic[8–24] and sometimes even "single-zeroth-order-state"[25] ensembles of molecules can be prepared above reaction thresholds. Thus, thermal broadening is eliminated, facilitating detailed studies of reaction dynamics. Unimolecular reactions induced by laser excitation are also amenable to product state analysis with unprecedented resolution,[8–24] and their dynamics can be monitored in the time domain.[26,27] Reflecting the experimental advances, theories such as variational RRKM[28–30] and the separate statistical ensembles (SSE) method[31] have offered new insights into such reactions, but much work still remains.

In order to calculate unimolecular reaction rates by using statistical theories, one needs the molecular density of states $\rho(E)$ and the number of open channels at the transition state $N^{\ddagger}(E - E_0)$, where E_0 is the threshold energy

$$k_{\text{uni}}(E) = \frac{N^{\ddagger}(E - E_0)}{h\rho(E)}. \qquad (1)$$

Due to incomplete knowledge of the potential energy surfaces of most reactions, $\rho(E)$ is usually estimated by extrapolating level positions that are determined spectroscopically near equilibrium. Such extrapolations are imprecise, and uncertainties also arise when considering the number of open channels at the transition state $N^{\ddagger}(E - E_0)$. Adjusting both the numerator and denominator of Eq. (1) guarantees that data can be fit for a given set of conditions, but does not challenge the underlying premises and may limit one's ability to extrapolate to energy regimes where there are no or limited data.

Statistical theories may be subjected to more stringent tests, even without knowing the exact potential energy surfaces. For this, state densities at high energies (as close to reaction threshold as possible) should be assessed experimentally and calculated reaction rates should be compared to experimental values near threshold, i.e., where only the first few transition state levels are involved. From this point of view, NO_2 is a good candidate for comparing experiment and theory, particularly since $\rho(E)$ near reaction threshold can be obtained experimentally, as described below. Specifically, it is a triatom with a potentially simple transition state structure (i) a high frequency NO-stretch vibration that is inaccessible over a broad energy range; (ii) a low frequency bend or hindered rotor; and (iii) the reaction coordinate. A small system like this offers promise for unraveling the underlying sources of statistical behavior. It is our premise that to understand *why* molecules behave statistically, it is necessary to see fine details that are more difficult to resolve in larger molecules.
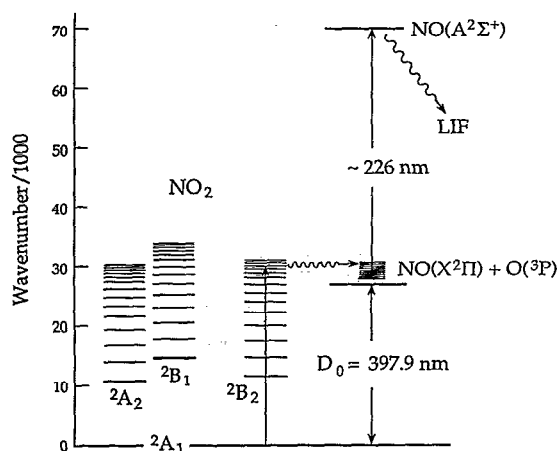
Because of the complexity of its electronic structure,

FIG. 1. Partial energy level diagram showing relevant NO$_2$ electronic states and NO product detection. Though the $^2B_1 \leftarrow ^2A_1$ transition has been observed, it is considerably weaker than $^2B_2 \leftarrow ^2A_1$ and therefore is not shown in the diagram.

there have been numerous publications on NO$_2$ spectroscopy.[32–48] It is well documented that the $^2A_1$ ground electronic state has a conical intersection with the lowest $^2B_2$ excited state, resulting in what is referred to as vibronic chaos above ~16 000 cm^{-1}.[43] Due to the $^2B_2$ character, these strongly mixed states are spectroscopically accessible over a broad range of wavelengths starting from the near-IR and extending well into the UV. It is the $^2A_1$ ground electronic state character of the optically excited states that guarantees access to unimolecular decay channels near threshold. Of course, the same spectroscopic features that make the reaction dynamics (unimolecular or otherwise) amenable to thorough experimental examination also complicate interpretation. Of particular concern is how the strong mixing of the $^2A_1$ and $^2B_2$ electronic states affects the dynamics. Moreover, two other electronic states, $^2A_2$ and $^2B_1$, are present in the energy region of the dissociation threshold.[46,48] Though these states are coupled to the lower ones by Coriolis and spin–rotation interactions, fluorescence lifetime analyses[35,37] and density of states considerations suggest that the spectroscopically accessible states possess predominantly $^2A_1$ and $^2B_2$ electronic character, at least in the threshold region. A partial energy level diagram showing relevant features is presented in Fig. 1.

A single quantum of near-UV radiation provides enough energy to surmount the dissociation threshold, which is known very accurately and is equal to the bond dissociation energy $D_0 = 25\,130.6$ cm^{-1}.[20,35] Just above threshold, decomposition proceeds to the ground electronic state products NO($^2\Pi_\Omega$; $\Omega = 1/2, 3/2$) and O(^3P_J; $J = 2, 1, 0$), where the subscripts denote fine structure levels. At much higher photon energies, the $^2B_2$ exit surface correlating with electronically excited products NO($^2\Pi_\Omega$) +O(^1D_J) may be accessible.[44,45] A number of groups have examined NO$_2$ ultraviolet photofragmentation in some detail, reporting center-of-mass (c.m.) kinetic energy distributions obtained from time-of-flight analyses,[49] and state

resolved product yields of NO($^2\Pi_\Omega$),[18–24] as well as O(^3P_J).[21,22] Lifetimes of NO$_2$ excited above the dissociation threshold have been estimated indirectly from angular distributions of the decomposition fragments,[49,50] resonance Raman spectroscopy,[36] and photofragment yield spectra.[20,22] Very recently, Reisler and co-workers[51,52] have shown that nascent vibrational and rotational level distributions have statistical signatures, including fluctuations in level densities due to interferences, the so-called Ericson fluctuations.[53]

Several recent spectroscopic studies provide the information needed to obtain the density of states near D_0. Delon *et al.* have successfully assigned resonance Raman spectra that involve vibrational levels of the ground electronic state up to 10 000 cm^{-1}.[42] By using these measured state densities, they extrapolate $\rho(E)$ from 10 000 cm^{-1} to higher energies, and in addition, have measured spectroscopically the density of optically accessible vibronic states in the region 16 500–18 500 cm^{-1}.[43] The extrapolated and measured state densities are in reasonable agreement, and from 18 500 cm^{-1}, it is possible to further extrapolate the density of states to the D_0 region (~25 000 cm^{-1}). Finally, detailed LIF spectra of very cold samples (i.e., ~1 K, having only the lowest rovibronic states occupied) have been reported in the vicinity of the dissociation threshold by Miyawaki *et al.*[22]

Based on this extensive body of data, the density of states near reaction threshold can be determined more reliably for NO$_2$ than for most molecules, thus facilitating tests of statistical transition state theories. Specifically, the independent measurements of Delon *et al.* and Miyawaki *et al.* give vibronic densities of states (ρ_{EV}) near D_0 of 0.2 and 0.3 per cm^{-1}, respectively, as discussed below. This difference is modest and we take these results to be in reasonable agreement with one another. With $\rho_{EV}(E)$ established by these independent experiments, the threshold reaction rate predicted from statistical theory is given by $k_{uni}(N^{\ddagger} = 1) = [h\rho_{EV}(E)]^{-1}$. For $\rho_{EV}(E) = 0.3$ per cm^{-1}, the threshold rate is 1×10^{11} s^{-1}. Thus, on the basis of Eq. (1), the threshold rate should have a well-defined, measurable value that cannot be made smaller by tuning closer to D_0. As shown below, this is exactly the behavior observed in our measurements.

Past experimental results on NO$_2$ photochemistry near D_0 have been analyzed using statistical reaction rate theories, and in fact, have been central to the development and refinement of such theories.[5–7,54–56] For example, in a pioneering study by Troe and co-workers, high pressure 300 K samples containing NO$_2$ were photolyzed at a number of different ultraviolet wavelengths, yielding the variation of the decomposition lifetime vs the wavelength of the photolyzing light.[54] Under these conditions, energized molecules can either dissociate or be collisionally deactivated to levels below D_0, so the measurements give the relative rates for these two processes. Thus, by estimating deactivation rates, the reaction rates were obtained, albeit indirectly. These rates were reconciled quite well by using the statistical adiabatic channel model.[5,6]

By combining the k_{uni} vs wavelength results of Troe

and co-workers[54] with a threshold (i.e., $N^{\ddagger}=1$) rate of 1×10^{11} s^{-1} inferred from the experimentally determined vibronic density of states near D_0,[22,42,43] it follows from Eq. (1) that resolvable steps in k_{uni} vs E can be observed experimentally. However, to achieve this, it is necessary to use expansion cooled samples in order to avoid washing out the desired effect by the spread in parent rotational excitation. Thus, we carried out direct time resolved measurements of NO_2 reaction rates using both expansion cooled and room temperature samples. The rates obtained with expansion cooled samples show a threshold rate of 1.6×10^{11} s^{-1}, which is in reasonable accord with the experimentally based values of $[h\rho_{EV}(D_0)]^{-1}$, and an irregular increase with energy, having spacings of ~ 100 cm^{-1}. This is referred to hereafter as "step-like" for lack of a more useful descriptive term. This behavior is in agreement with the variation suggested by Eq. (1). Thus, it appears that NO_2 displays features of the "transition state" via its $k(E)$ dependence. This constitutes an advance in our ability to probe features of the transition state.

In contrast to rotationally cold samples, the rates measured with room temperature gas show a smooth variation of rate vs photolysis wavelength with higher decay rates at each photolysis wavelength than for expansion cooled samples. This is anticipated because of the additional energy of the thermally occupied NO_2 rotations. These results are in good agreement with the indirect measurements of Troe and co-workers.[54] It appears that the NO_2 molecule may serve us well as a prototype of triatomic unimolecular decomposition. Other small molecules that display $k(E)$ structure such as ketene[16,17,57] can also be expected to serve as prototypes for detailed unimolecular decomposition studies.
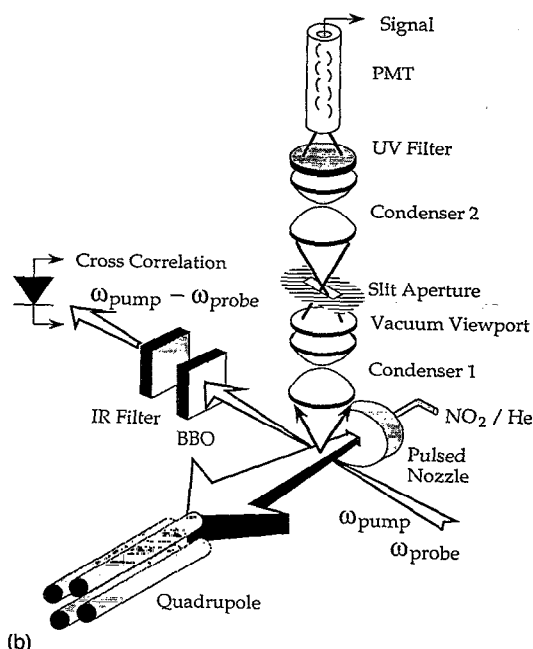
II. EXPERIMENT

The experimental arrangement is shown schematically in Fig. 2. The main parts are (i) a dual-jet mode-locked dye laser (Coherent 702-1), synchronously pumped by the frequency doubled output of (ii) an actively mode-locked Nd:YAG laser (Spectron SL 903); (iii) two dye amplifiers pumped by (iv) a regenerative Nd:YAG amplifier (Continuum RGA 69-10); and (v) a vacuum chamber equipped with a pulsed nozzle, quadrupole mass spectrometer and accessories for monitoring LIF. The mode-locked Nd:YAG laser with a computer-aided measurement and control (CAMAC) ML 4000 mode locker generates a train of 100 ps pulses at 76 MHz; typical average power is 20 W at 1064 nm. A 5% portion of this radiation is used for seeding the regenerative amplifier, the remaining 95% is frequency doubled in a 12 mm LBO crystal producing about 2 W of 532 nm radiation for dye laser pumping.

Table I presents the combinations of gain and saturable absorber dyes used in the dual-jet dye oscillator and first amplifier. Using a single-plate birefringent filter (BRF) as a tuning element, 250–500 fs pulses tunable from 575 to 645 nm with ~ 40–70 cm^{-1} spectral bandwidth are obtained from the mode-locked dye laser. The shortest pulses are observed on the red side of the covered spectral range. Replacing the single-plate BRF by a double-plate
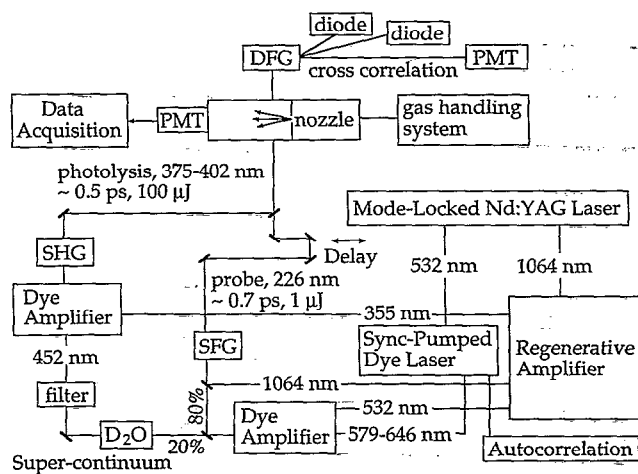
(a)

(b)

FIG. 2. (a) A schematic diagram of the experimental arrangement emphasizing the generation of the pump and probe pulses. (b) A schematic diagram illustrating the pulsed nozzle, mass spectrometer, and optical arrangement.

TABLE I. Gain and saturable absorber (SA) dyes used in the dual jet oscillator and first amplifier. Also shown are Schott glass filters used as solid state saturable absorbers (SSSA) in the first amplifier to minimize pulse broadening.

Wave-length (nm)	Oscillator dyes		Amplifier dyes	
	Gain	SA	Gain	SSSA[a]
575–595	Rh590(*Cl*)	DODCI/DQOCI	Rh610	RG610
595–605	Rh590(*Cl*)	DODCI/DQTCI	*K* red (H_2O) or *S* Rh640 (MeOH)	RG630
605–618	*K* red	DQTCI	DCM (MeOH) or *S* Rh640 (MeOH)	RG645
618–645	*K* red/ *S* Rh640	DQTCI	DCM (MeOH)	RG665

[a]Three millimeters long.

Pump Pulses

Single-Plate BRF

Double-Plate BRF

| | | | |
396   397   398   399
Wavelength/nm

Probe Pulse

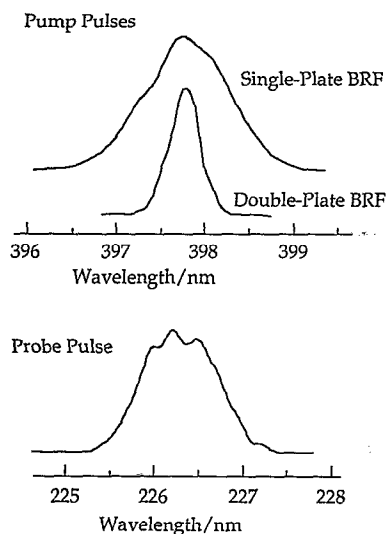| | | | |
225   226   227   228
Wavelength/nm

FIG. 3. Sample spectra of pump and probe pulses measured by a SPEX 1461 double monochromator with 0.15 cm^{-1} spectral resolution. The two pump spectra correspond, as indicated, to single or double plate BRF configurations of the mode-locked dye laser; the corresponding pump–probe cross correlations are, respectively, 0.7 and 1.3 ps FWHM.

BRF results in the bandwidth narrowing to ~40% of its original value, as shown in Fig. 3, which presents sample spectra of the pump beam for single and double plate BRFs. This narrowing is accompanied by broadening of the temporal pulse width. Although 300 mW is obtained at the exit of the dual-jet dye laser, only half of this is used for successive amplification in order to minimize pulse broadening.

The output pulse train from the dye laser is amplified in a three-stage amplifier (Continuum PTA-60). The amplifier is longitudinally pumped at 10 Hz by the second harmonic of the RGA which typically provides 30 mJ, 80 ps pulses at 532 nm. A solid state saturable absorber (see Table I) is positioned between the first and the second amplification stages for reducing pulse broadening. The amplified dye laser pulse, which reaches 2 mJ without noticeable broadening, is divided into two beams by a broadband beam splitter. The first beam, containing ~80% of the energy, is spatially matched using a telescope and then combined on a dichroic mirror with a 1064 nm, 50 mJ beam from the RGA. These beams are mixed in a 1 mm BBO crystal producing ~200 μJ of sum frequency radiation tunable from 373 to 402 nm. No significant broadening is observed in this near-UV pulse, as ascertained from its cross correlation with the dye laser fundamental. The cross correlation is measured by sum frequency generation in a 150 μm BBO crystal. The near-UV pulse is used to excite NO$_2$ molecules over the dissociation threshold causing their decomposition.

The remaining 20% of the amplified dye laser fundamental is focused by a 10 cm f.l. lens into a D$_2$O cell producing a white continuum. To avoid boiling, the heavy water is constantly stirred by a magnetic stirrer. Vertically polarized 452 nm radiation (~1 nJ, 6 nm bandwidth) is selected from the continuum by a Corning 5-57 glass filter followed by a Glan–Taylor polarizer and an interference filter. These components are positioned behind a 8 cm f.l. lens which recollimates the light exiting the D$_2$O cell. Autocorrelation traces of the filtered continuum show ~50% temporal broadening of the 452 nm pulses as compared to the dye laser fundamental. This broadening is due mainly to the interference filter and is minimized by reducing white light divergence. The 452 nm radiation is amplified in a second PTA-60, pumped by the third harmonic of the RGA (355 nm, 45 mJ, 80 ps). Though the PTA-60 is designed for longitudinal pumping, such a configuration does not provide satisfactory performance in the 450 nm region because of the low gain of blue dyes. Therefore, the three-stage amplifier has been modified for transverse pumping. The first, second, and last stages are pumped, respectively, by 5%, 5%, and 90% of the available 355 nm radiation. The pump beams are focused into the dye cells by 5 cm f.l. cylindrical lenses. The positions of the lenses are individually adjusted for matching the amplified beam, which has different cross sectional diameters in each stage. We use coumarin 460/MeOH in the first and final stages with 5.5 and 1.5×10^{-4} M concentrations, respectively. To minimize ASE, coumarin 440 (2.5×10^{-4} M in methanol) is used in the second stage. Because of the changed beam geometries in the modified amplifier, the pinhole spatial filter has been removed from its original position between the first two stages. The modified amplifier provides 200 μJ at 452 nm; the amplified beam diameter is ~6 mm. The amplified 452 nm beam is frequency doubled in a 150 μm thick BBO crystal, and the resulting 226 nm pulse is used to probe NO products via LIF using the γ system. The bandwidth of the probe pulse, which is shown in the lower panel of Fig. 3, is large enough for monitoring virtually all NO rotational levels.

After passing through a computer-controlled delay stage (Aerotech ATS100), the pump beam is combined with the probe radiation on a dichroic mirror and collinearly focused by a 30 cm f.l. lens into a vacuum chamber pumped to 10^{-6} Torr. The chamber is equipped with a pulsed nozzle (250 μs duration, 500 μm diam. orifice), a quadrupole mass spectrometer for monitoring the beam intensity, a leak valve and an MKS Baratron 122*A* pressure meter for the gas flow experiments, and a photomultiplier tube (PMT) (Hamamatsu R943-02) and associated collection optics for LIF measurements. In experiments employing expansion-cooled samples, the collinear laser beams intersect the supersonic jet ~40 nozzle diameters downstream from the nozzle. A 3% NO$_2$/He gas mixture is prepared *in situ* by blowing 1 atm of He over a NO$_2$ sample frozen at −28 °C. A 760 Torr stagnation pressure is kept throughout the measurements. As shown by Robra *et al.*,[20] such expansion conditions produce rotationally cold NO$_2$ molecules with ~6 K rotational temperature. The NO$_2$ sample (Matheson, 99.5%) is purified prior to each set of experiments by bubbling O$_2$ through 0 °C nitrogen dioxide liquid followed by several freeze–pump–thaw cycles. The prepared sample is kept under 1 atm of O$_2$ between experimental runs in order to bias the NO$_2$⇌NO + (1/2)O$_2$ equilibrium towards NO$_2$. To further minimize
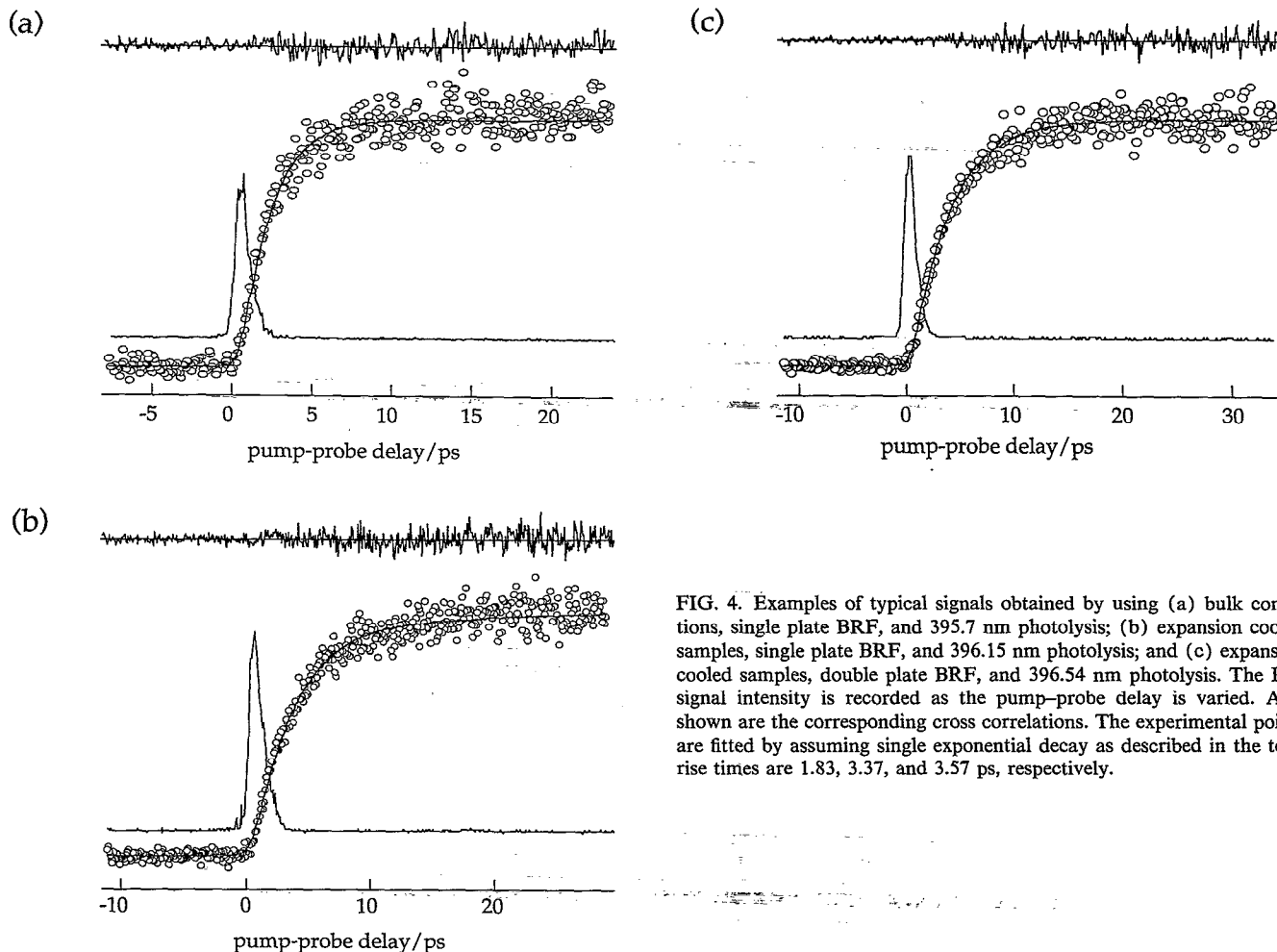
(a)

(b)

(c)

FIG. 4. Examples of typical signals obtained by using (a) bulk conditions, single plate BRF, and 395.7 nm photolysis; (b) expansion cooled samples, single plate BRF, and 396.15 nm photolysis; and (c) expansion cooled samples, double plate BRF, and 396.54 nm photolysis. The LIF signal intensity is recorded as the pump–probe delay is varied. Also shown are the corresponding cross correlations. The experimental points are fitted by assuming single exponential decay as described in the text; rise times are 1.83, 3.37, and 3.57 ps, respectively.

NO$_2$ decomposition, the nozzle interior is coated with Teflon and the portion of the gas system between the NO$_2$ bath and the nozzle is kept at −20 °C. Room temperature samples are prepared by flowing NO$_2$ gas through the vacuum chamber at a sufficient rate for replenishing the sample between laser shots. The total pressure in the flow, typically 30–60 mTorr, is measured with a Baratron manometer, recorded in a computer, and then used for normalizing the LIF signal. Sample preparation and gas handling are similar in the gas flow and supersonic jet experiments.

The NO LIF signal is preamplified, digitized, and collected in an IBM AT computer simultaneously with both pump and probe pulse energies and a pump–probe cross correlation signal. The cross correlation is obtained by difference frequency generation in a 100 μm BBO crystal which is positioned shortly after the chamber. The pump, probe, and difference frequency radiations are separated in a 60° quartz prism and detected by two UV-grade photodiodes and a PMT, respectively.

III. RESULTS

Representative scans of NO LIF signal vs the delay between the pump and probe pulses are shown in Fig. 4 for expansion cooled and room temperature samples, respectively. There are typically 300–500 data points (circles) in

each trace, and each of the circles represents an average over 20 laser shots and is normalized to the pump and probe energies. Also shown in Fig. 4 are examples of pump–probe cross correlations which were recorded by difference frequency generation simultaneously with the LIF signal. The LIF signals and cross correlations were recorded simultaneously for *all* of the data presented in this paper. We have verified experimentally that the NO LIF signal is a linear function of both pump and probe laser energies and that the experimentally determined decay rates are independent of the pump energies. Therefore, the observed photodecomposition of NO$_2$ is the result of a one photon process.

The experimental time dependencies $S(t)$ are fit by assuming single exponential NO production

$$S(t) \propto \int_{-\infty}^{t} ds\, R(s)\{1-\exp[-k_{\text{uni}}(t-s)]\}, \quad (2)$$

where

$$R(s) = \int_{-\infty}^{\infty} dt\, I_{\text{pump}}(t) I_{\text{probe}}(t-s) \quad (3)$$

represents the measured cross correlation between the pump and probe pulses and k_{uni} is an adjustable parameter describing unimolecular reaction. Equations (2) and (3) implicitly neglect coherent effects in pumping and probing.
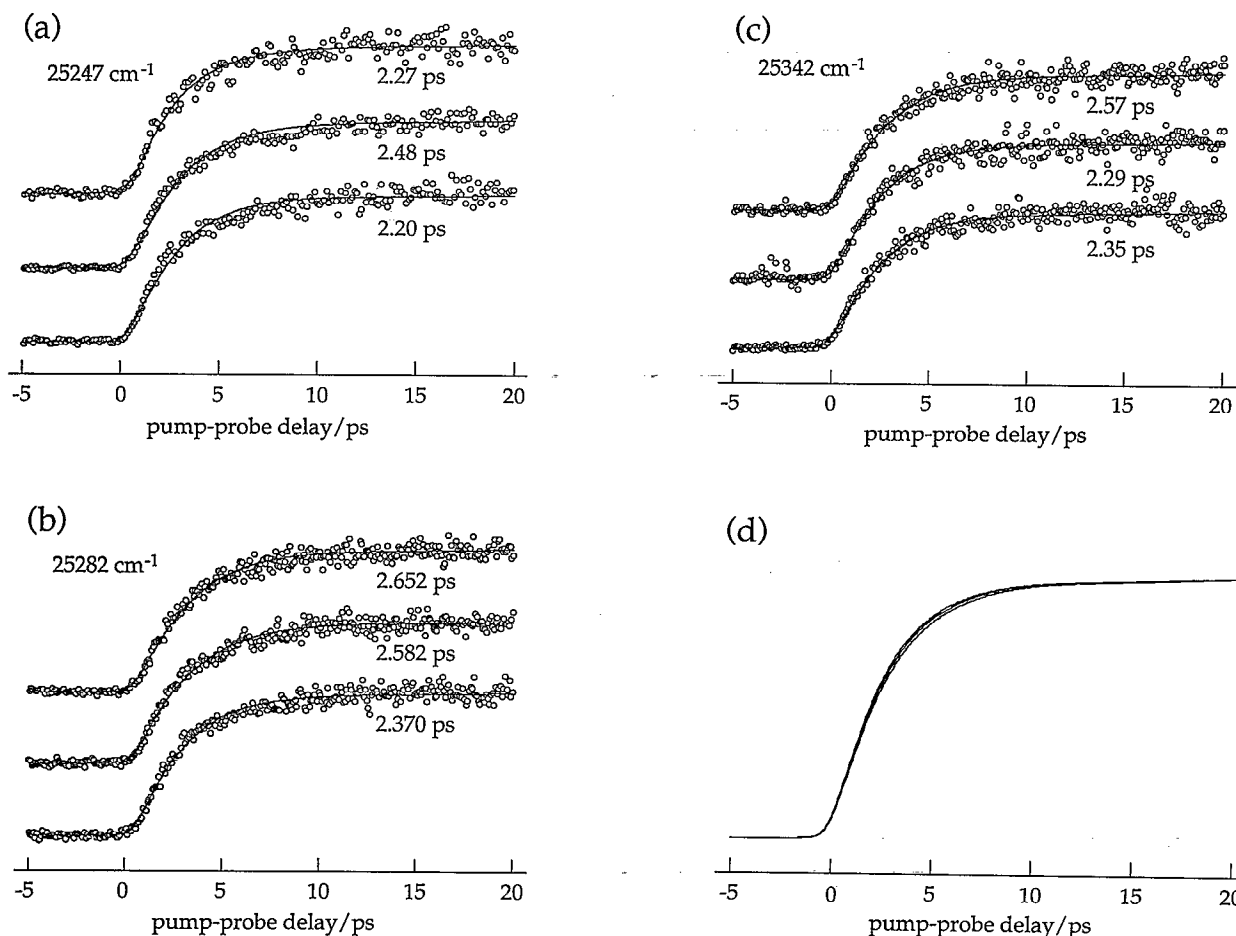
FIG. 5. LIF signal vs pump–probe delay for excitation at 25 247, 25 282, and 25 342 cm^{-1}. (a)–(c) each show three representative traces and the corresponding k_{uni} values. Typically, ten such traces are recorded at a single excitation wave number; all are similar in appearance. The solid line is the fit obtained by using Eqs. (2) and (3). (d) gives a superposition of three traces that use the averaged k_{uni} values listed in Table II for the three wave numbers given above and a 1.0 ps FWHM cross correlation width. The curves are almost indistinguishable.

A detailed analysis of coherent effects for our experimental conditions will be given elsewhere. Briefly, the above assumption is justified for the present laser pulses, which have approximately five times larger spectral widths than transform limited pulses of the same temporal duration. Additionally, unimolecular decay can be expected to yield products that have poor phase coherence.

Fits of the data by the above convolution are shown as solid lines in Fig. 4. As seen from the figure, the assumption of a single exponential provides good agreement; small discrepancies between the data and the simulations are not serious. We note that the spectral bandwidths of the pump pulses (i.e., 20–80 cm^{-1}) are sufficient to excite 40–160 molecular eigenstates for an assumed rovibrational density of states of 2 per cm^{-1}, as discussed in Appendix A. Since state-to-state dissociation rates are expected to fluctuate,[25] modest deviations from single exponential decay are not surprising.

Representative data for the case of expansion cooled samples are presented in Figs. 5 and 6. Each of the entries labeled (a), (b), and (c) contain three traces. A single trace requires about 20 min to record and the cross correlation widths vary some between traces (e.g., 0.6–1.2 ps

with the single-plate BRF and 1.5–2 ps with the double-plate BRF). The reason for presenting several traces in each entry is to emphasize the repeatability of measurements taken at a particular photolysis wave number and bandwidth—these were carried out over periods ranging from days to weeks. For example, Fig. 5(a) shows three traces obtained with the photolysis wave number centered at 25 247 cm^{-1} and with a bandwidth of 28 cm^{-1} (two-plate BRF, 1.5 ps cross correlation). The single-exponential k_{uni} values obtained from Eqs. (2) and (3) are placed next to the corresponding traces. For the sake of brevity, only three traces are shown though ten were taken under the conditions of Fig. 5(a); all are of similar quality.

At each of the photolysis wave numbers, averaging of the individual k_{uni} values obtained from traces such as those shown in Figs. 5 and 6 yields a single k_{uni} value. These are presented in Table II for the different excitation wave numbers. Standard deviations are small, as shown in the table.

Figure 5(d) displays traces that correspond to averaged k_{uni} values obtained at 25 247, 25 282, and 25 342 cm^{-1}. For each average value of k_{uni}, the function $[1-\exp(-k_{uni}t)]$ is convoluted with a cross correlation
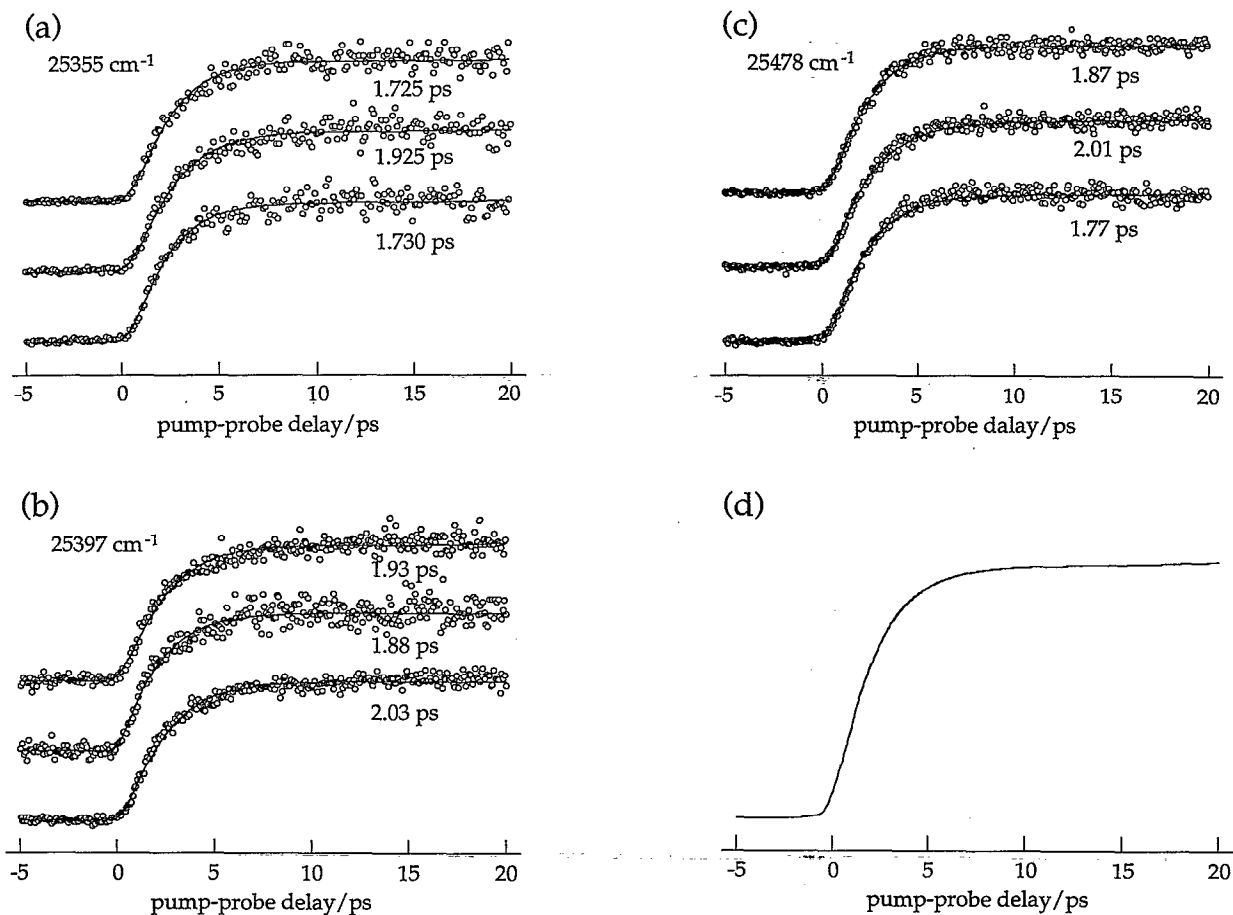
FIG. 6. LIF signal vs pump–probe delay for excitation at 25 355, 25 397, and 25 478 cm^{-1}; details are the same as for Fig. 5. In (d), the three curves are indistinguishable.

that is the same [1.0 ps full width at half-maximum (FWHM)] for each k_{uni} value. The three curves lie so close to one another that they are almost indistinguishable. A similar situation exists for the k_{uni} values obtained at 25 355, 25 397, and 25 478 cm^{-1}, as shown in Fig. 6. The superposition of the three curves corresponding to these excitation wave numbers [see Fig. 6(d)] shows that the rates are truly indistinguishable at the present experimental resolution.

From a perusal of the results presented in Figs. 5 and 6 and summarized in Table II, it is clear that the k_{uni} values are essentially the same (4.1×10^{11} s^{-1}) for the energies in excess of reaction threshold $E^\dagger = 120$, 150, and 210 cm^{-1}. Similarly, the k_{uni} values are essentially the same (5.4×10^{11} s^{-1}) for the $E^\dagger$ values 225, 240, 270, and 350 cm^{-1}. On the other hand, these two rates differ by an amount that is outside the statistical uncertainty; i.e., due to the large amount of averaging, random fluctuations are modest, as shown in Table II. Figure 7 makes this point by showing the rates for the six $E^\dagger$ values used in Figs. 5 and 6. The abrupt change in $k_{uni}(E)$ displayed in Fig. 7—remaining approximately constant, then jumping from 4.1×10^{11} to 5.4×10^{11}, then remaining approximately constant—is what we refer to as "step-like" behavior. Though such fea-

TABLE II. Unimolecular decay rates for expansion cooled NO$_2$; also presented are parameters of the laser pulses $\delta\nu_{pump}$—the FWHM bandwidth of the pump pulse, $\delta\tau_{xcor}$—the FWHM width of the pump–probe cross correlation, and σ_k—the statistical uncertainty from independent scans.

$h\nu_{pump}$ (cm^{-1})	$h\nu - D_0$ (cm^{-1})	k_{uni} (ps^{-1})	$\delta\nu_{pump}$ (cm^{-1})	$\delta\tau_{xcor}$ (ps)	σ_k (ps^{-1})
25 126[a]	−5	b	31	1.5	b
25 139[a]	7	0.16	25	1.3	0.02
25 140	8	0.15	70	0.7	0.01
25 190	59	0.20	45	0.8	0.02
25 218[a]	87	0.28	20	1.3	0.01
25 243	112	0.29	55	1.2	0.01
25 247[a]	116	0.42	28	1.3	0.03
25 282	151	0.39	58	0.9	0.03
25 342	211	0.41	·65	1.0	0.03
25 355[a]	224	0.53	28	1.3	0.05
25 368[a]	237	0.58	29	1.1	0.07
25 397	266	0.53	58	0.8	.0.04
25 478	347	0.53	77	0.9	0.05
25 550	419	0.58	67	0.9	0.04
25 630	499	0.68	80	1.1	0.07
25 750	619	1.10	60	1.1	0.16
25 969	838	1.32	55	1.1	0.48
26 126	995	2.76	30	1.0	0.90

[a]Obtained with the double-plate BRF.
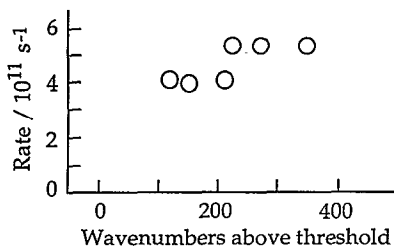[b]Decomposition is not observed with this pump radiation.

FIG. 7. The six averaged k_{uni} values associated with the excitation wave numbers for Figs. 5(a)–5(c) and 6(a)–6(c) are shown. Note the step 4.1×10^{11} s^{-1} jumping to 5.4×10^{11} s^{-1}.

tures are not resolved well enough to be described quantitatively, they are definitely present. Figure 8 shows traces analogous to those presented in Figs. 5(d) and 6(d). The difference, while not large, is clear.

With expansion cooled samples, a pronounced threshold for NO$_2$ photodecomposition is observed, with fragmentation occurring at pump wave numbers above 25 130 cm^{-1}. This agrees with the reported threshold for NO$_2$ decomposition of 25 130.6 cm^{-1}.[20,34] To discern the threshold rate to the extent possible with our broad pump laser bandwidth of ~20 cm^{-1}, the following experiment was done: The pump was set at 25 130 cm^{-1} and the rise time was recorded. The pump laser was then tuned to smaller wave numbers while recording the rise times. This has the effect of reducing the size of the signal, since less and less of the 20 cm^{-1} pump bandwidth is above the reaction threshold. However, even though the signal amplitude decreased and eventually went to zero, within the experimental uncertainty, the rise times remained constant at ~1.6×10^{11} s^{-1}. Thus, we take this to be the threshold rate corresponding to $N^{\ddagger} = 1$ in Eq. (1), as viewed with coarse frequency resolution. With substantially better spectral resolution, it may be possible to resolve smaller rates just at threshold.

On the other hand, room temperature samples do not exhibit an abrupt energy threshold. As the pump wave number is decreased from 25 130 cm^{-1}, the reaction yield decreases monotonically and finally disappears at ~24 880 cm^{-1}. It should be pointed out that the vibronic energy of

FIG. 9. Unimolecular decay rate vs the quantity $h\nu$-D_0 (i.e., essentially the energy in excess of reaction threshold) for expansion cooled samples. The rectangle lengths represent the spectral bandwidths of the corresponding pump pulses. Statistical uncertainties (see Table II) lie within the rectangle heights.

photoexcited molecules is essentially the same as the photon energy because at $T = 300$ K, approximately 97% of the molecules reside in the ground vibrational level (the lowest NO$_2$ vibrational frequency is 758.6 cm^{-1}).[42] Therefore, for a given photon wavelength, decay rates measured with room temperature and expansion cooled samples correspond to nearly the same initial vibronic energy, but to different initial rotational distributions, i.e., 300 vs ~6 K. The 6 K rotational temperature of expansion cooled NO$_2$ has been estimated from the data of Robra *et al.*[20] who employed similar expansion conditions. Thus, differences in the photoinduced decomposition rate of NO$_2$ should be attributed to the different initial rotational energies.

A summary of the unimolecular decay rates extracted from the experimental delay time dependences is presented in Figs. 9 and 10 as well as Tables II and III. Each point in the figures and each entry in the tables is an average of eight to 16 rates obtained from independent scans at the
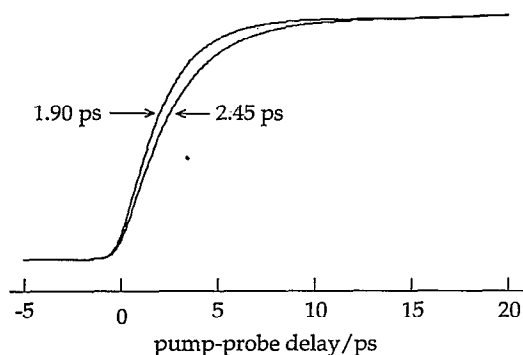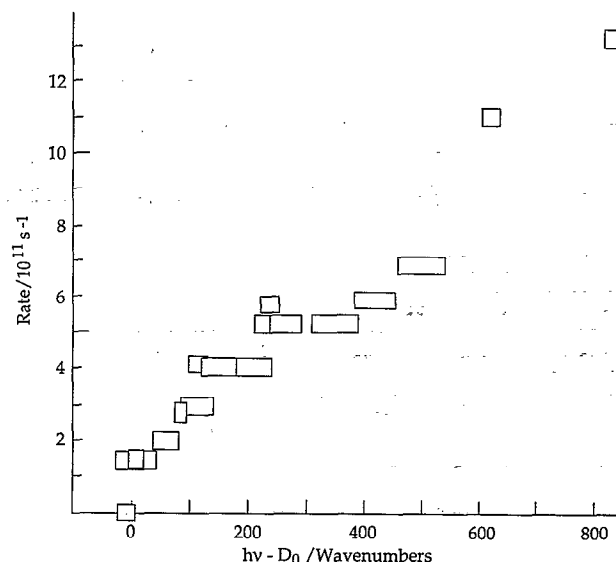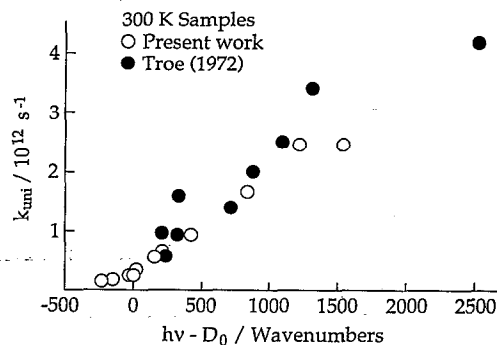

FIG. 8. The function $[1 - \exp(-k_{uni}t)]$ is convoluted with a 1.0 ps FWHM cross correlation for the rates at each of the steps shown in Fig. 7.

FIG. 10. Unimolecular decay rate vs the quantity $h\nu$-D_0 for room temperature samples.

TABLE III. Unimolecular decay rates measured for room temperature NO$_2$; notations for laser pulses parameters are the same as in Table II.

$h\nu_{pump}$ (cm^{-1})	$h\nu - D_0$ (cm^{-1})	k_{uni} (ps^{-1})	$\delta\nu_{pump}$ (cm^{-1})	$\delta\tau_{xcor}$ (ps)	σ_k (ps^{-1})
24 894[b]	−237	0.17	37	1.7	0.01
24 975[b]	−156	0.19	40	2.3	0.02
25 095[a]	−36	0.26	25	1.6	0.03
25 126[a]	−5	0.28	31	1.5	0.04
25 139[a]	8	0.36	25	1.6	0.02
25 275	144	0.57	170	0.9	0.04
25 331	200	0.65	125	1.0	0.06
25 545	414	0.94	104	1.1	0.15
25 954	823	1.7	84	1.1	0.3
26 325	1194	2.5	82	1.0	0.7
26 656	1525	2.5	78	1.0	0.8

[a]Obtained with the double-plate BRF.
[b]Obtained with a single-plate BRF and without a saturable absorber in the cw dye laser.

excitation wave number. The widths of the rectangles indicate the pump laser bandwidths; statistical uncertainties lie within the heights of the rectangles. Figure 9 shows decomposition rates measured with expansion cooled samples, while Fig. 10 shows rates measured with room temperature samples as well as the earlier results of Troe and co-workers.[54] Obviously rotating molecules decompose faster at a specific photolysis wave number than those rotationally cooled in the expansion.

Figure 9 shows a detailed view of the decay rates for rotationally cooled samples. It should be noted that independent measurements have been carried out for several excitation wavelengths near reaction threshold with either one or two birefringent filters in the mode-locked dye oscillator. As discussed in the previous section, the single-plate BRF provides better time resolution, i.e., as low as 0.5 ps FWHM cross correlation, but with relatively low spectral resolution (40–70 cm^{-1}) compared to the double-plate BRF, which provides ~1.5 ps cross correlation and 20–30 cm^{-1} spectral resolution.

One aspect of the results obtained with expansion cooled samples is noteworthy—k_{uni} vs photolysis wave number is not a smooth ascending function, as is usually the case for measured unimolecular decomposition rates, and as is the case for room temperature NO$_2$ samples. With expansion cooled samples, $k(E)$ exhibits several sharp rises that cannot be attributed to low S/N. When this was discovered, it was checked carefully for many months before we concluded that it was a signature of the elusive transition state.

IV. DISCUSSION

A. $k_{uni}(E)$ structure for expansion cooled NO$_2$

Though a step-like increase of the unimolecular decay rate with energy has been anticipated for a long time, the first direct time domain observations of such an effect were reported only recently. Zewail and co-workers noted a small irregularity in k_{uni} vs E for photoinitiated NCNO decomposition,[26] which has been shown to be a classic case

of unimolecular reaction.[58] More prominent effects were observed by our group for NO$_2$,[59] and independently by Moore and co-workers for ketene.[57]

As stated in the Introduction, the simplest form of the microcanonical RRKM theory uses Eq. (1) to compute $k_{uni}(E)$,

$$k_{uni}(E) = \frac{N^{\ddagger}(E-E_0)}{h\rho(E)}, \tag{1}$$

where E_0 (the reaction threshold) is essentially D_0 for the case of expansion cooled samples, since centrifugal barriers are minimal and there is no reverse barrier. As the energy exceeds the reaction threshold, $N^{\ddagger}(E-E_0)$ changes from zero to one. Then it jumps from one to two when two channels become available, etc. Since $\rho(E)$ changes much more slowly than $N^{\ddagger}(E-E_0)$, Eq. (1) predicts a step-like increase of k_{uni} with energy. Such steps are also expected from general considerations that relate them to open channels at the transition state.[60]

B. Fluctuations and averaging

It is tempting to attribute the observed $k(E)$ structure to the number of open channels and thus obtain level positions for the transition state. However, caution is needed, since the pump laser pulse, even with its broad bandwidth, excites a modest number of NO$_2$ states. Consequently, an explanation that attributes the observed $k_{uni}(E)$ dependence to state-to-state fluctuations in the reaction rate should not be dismissed *a priori*. Fluctuations of near-threshold reaction rates have been observed recently in the unimolecular decomposition of formaldehyde,[25] and Miller *et al.*[61] have shown that for the decay of single zeroth order states of the reactant, the average rate ($\langle k_{uni} \rangle$) and distribution width for the fluctuations [$\sigma = (\langle k_{uni}^2 \rangle - \langle k_{uni} \rangle^2)^{1/2}$] are related to the number of independent decay channels in the transition state

$$\sigma = \langle k_{uni} \rangle (2/N^{\ddagger})^{1/2}. \tag{4}$$

In the present experiments, the measured rates do not correspond to reactions of individual zeroth order states, but are averages over those states that are optically accessible to the pump pulse, i.e., within $\rho(E)\delta E_{pump}$, where δE_{pump} is the pump bandwidth. As shown in Appendix A, for each value of the angular momentum quantum number J,

$$\rho(E,J) = (2J+1)\rho_{EV}(E,B_2), \tag{5}$$

where $\rho(E,J)$ is the density of rovibronic states with J specified and $\rho_{EV}(E,B_2)$ is the density of B_2 vibronic levels. As a result of averaging, the scatter of the measured rates from one pump wavelength to another is reduced by $m^{1/2}$, where m is the number of NO$_2$ states within δE_{pump}. This gives a width of

$$\sigma_m = \frac{\langle k_{uni} \rangle}{[\Sigma_J \rho(E,J)\delta E_{pump} N^{\ddagger}(E-E_0,J)/2]^{1/2}}, \tag{6}$$

where

$$N^\ddagger(E-E_0,J) = (2J+1)N_{EV}^\ddagger(E-E_0,B_2) \qquad (7)$$

is the number of accessible transition state levels for each J and $N_{EV}^\ddagger(E-E_0,B_2)$ is the number of vibronic levels. Equation (6) implicitly assumes that levels are optically excited with equal probability. Application of Eq. (6) gives $\sigma_m \leqslant 0.1 \langle k_{uni}\rangle$ near threshold for values of $\rho_{EV}(D_0,B_2)\delta E_{pump}$ ranging from 7 to 30, and with $J=2.5$ (i.e., the most probable J at 6 K). Thus, statistical fluctuations are expected to be smaller than the symbols in the figures, so we conclude they are not responsible for the measured $k_{uni}(E)$ dependence.

C. Assigning the step-like behavior

From the above, it follows that the steps in the decomposition rate can be attributed to the opening of decay channels at the transition state; it remains to assign these channels. In a set of experiments by Moore and co-workers using expansion-cooled CH$_2$CO, step-like rises in the yield for the singlet channel were observed with energy increments corresponding to CO rotational levels.[16,17] It is noteworthy that the singlet channel does not have a barrier along the reaction coordinate, as opposed to the lower lying triplet channel. Zewail and co-workers, on the other hand, measured rates for CH$_2$CO decomposition on the singlet surface,[27] which were reconciled using variational RRKM theory with transition state parameters that included low frequency vibrations.[62] These calculations seem to contradict the experimental step spacing in the singlet yield. However, it is possible that the steps observed by Moore and co-workers in the singlet yield are due to competition between singlet and triplet exit channels past a rate limiting transition state. The triplet channel alone exhibits larger k vs E steps, suggesting a tight transition state.[57] Also, in experiments of Zewail and co-workers on NCNO decomposition, it was shown that the rates increased smoothly with energy except at one point;[26] again, a variational RRKM analysis employed low-frequency vibrations at the transition state.[63]

As stated earlier, the $k(E)$ step size for NO$_2$ can be inferred from a knowledge of $\rho_{EV}(E,B_2)$ and the variation of k with photolysis wavelength determined in 1972 by Troe and co-workers.[54] Though done in hindsight, the result is clear—the $k(E)$ slope can only be reconciled within the framework of Eq. (1) by a somewhat tight transition state. Thus, although the observed spacings of ~ 100 cm^{-1} for NO$_2$ are slightly higher than for similar cases of small molecules decomposing via loose transition states,[16,17,26,27,62,63] these observed spacings are consistent with the independent estimates of $\rho(E)$ and $k(E)$.[5]

These spacings may correspond either to transition state levels that correlate with atomic oxygen (i.e., $^3P_2$, $^3P_1$, and $^3P_0$ fine-structure levels at 0, 158, and 227 cm^{-1}, respectively, in the free atom),[64] or alternatively to a bending frequency at the transition state. Though the spacings between the oxygen levels are not equal to the observed separations between steps, such a possibility should not be excluded on this basis alone, since level positions in the transition state may be shifted relative to those in the free

atom. However, with such an assignment, we are still left to deal with the bending degree of freedom at the transition state and its implication on the rate. As mentioned above, the transition state bending vibration should be significantly lowered in frequency compared to 758.6 cm^{-1} near equilibrium in NO$_2$ and may even be representable as hindered rotation. If the vibrational level spacing at the transition state is relatively high, the corresponding steps should be observable in $k(E)$ in addition to those associated with the oxygen electronic levels. Experimentally, this is not observed, though it could easily be obscured by the low S/N. In the opposite case of low separations between vibrational or rotor levels, the steps would be too fine grained for our experimental resolution and would appear as a smooth increase of k_{uni} vs E. Neither is this observed. Moreover, this would be inconsistent with the measured $\rho(E)$ values, which preclude the possibility of such small step sizes. Thus, we favor a vibrational interpretation of the observed steps.

In the range of energies used in the present experiments, the transition state has only one accessible vibrational degree of freedom since the NO stretch is too energetic, i.e., 1876 cm^{-1} for free NO.[65] The NO$_2$ bend fundamental is 758.6 cm^{-1},[42] which will be lowered considerably at the transition state. Thus, we tentatively associate the rise near 100 cm^{-1} with opening of the $v=1$ bend in the transition state; likewise the step near 200 cm^{-1} is associated with $v=2$. These assignments are consistent with the rates at the second and third steps being roughly two and three times as large as the rate at the initial step. Finally, we note that the steps in k_{uni} vs E are prominent only up to ~ 350 cm^{-1}. As seen in Fig. 9, no steps are seen in the region where the reaction rates are fast compared to the experimental temporal resolution. Deteriorating experimental accuracy probably hides details of the $k_{uni}(E)$ dependence in this region. We leave this higher energy regime for further investigations.

D. RRKM estimations of $k_{uni}(E)$

Several concerns arise immediately in applying the RRKM theory. Though products are accessed via the ground electronic surface, as verified from product state distributions,[20,22] the overall reaction involves at least two strongly coupled zeroth order electronic surfaces.[44–48] Furthermore, our experimental technique capitalizes on $^2A_1/^2B_2$ mixing, which facilitates efficient NO$_2$ photoexcitation above dissociation threshold. Additionally, there are Coriolis and spin–rotation interactions between the $^2A_1$, $^2B_2$, $^2A_2$, and $^2B_1$ electronic states. However, $^2A_2$ and $^2B_1$ are of minor concern since density of states considerations as well as fluorescence lifetime analyses[35,37] indicate that the optically prepared states possess predominantly $^2A_1/^2B_2$ electronic character. More complications appear if rotational, vibronic, and spin angular momenta are not separable due to spin–rotation and Coriolis interactions. In summary, the molecular eigenstates contributing to $\rho(E)$ in Eq. (1) are not clear. Equation (1) follows from detailed balance[2,66] with $\rho(E)$ being the density of all molecular eigenstates coupled to products, i.e., the *total density*

of states for both electronic surfaces subject to energy, angular momentum, and parity conservation. Justification comes from the fact that NO$_2$ fluorescence vanishes if the molecule is excited over the threshold,[20,22] indicating that all optically prepared states dissociate (see also the next section).

Appendix A shows that the density of optically prepared NO$_2$ states near D_0 can be expressed as $\rho(E,J) = (2J+1)\rho_{EV}(E,B_2)$, where $\rho_{EV}(E,B_2)$ is the combined densities of B_2 vibrational levels on the $^2A_1$ surface and A_1 vibrational levels on the $^2B_2$ surface. Near D_0, $\rho_{EV}(E,B_2) \sim 0.3$ per cm^{-1} is estimated from LIF spectra of very cold NO$_2$, i.e., ~ 1 K, mainly having only the $J=1/2$ level initially populated.[22] In obtaining $N^\ddagger$, we take into account that the symmetry of optically prepared states is conserved throughout reaction. Also, we assume that Coriolis and spin–rotation interactions are at least as important in the transition state as in the parent molecule because the transition states are expected to be less rigid than the equilibrium configuration. Consequently, the number of transition state levels is obtained similarly to the density of states and is given by $N^\ddagger(E-E_0,J) = (2J+1)N^\ddagger_{EV}(E-E_0,B_2)$. In this case,

$$\frac{N^\ddagger(E-E_0,J)}{\rho(E,J)} = \frac{N^\ddagger_{EV}(E-E_0,B_2)}{\rho_{EV}(E,B_2)}. \qquad (8)$$

Therefore, the rate given by Eq. (1) may be calculated by counting vibronic states only. Though true for NO$_2$, this may not generally be the case, since the degree of mixing resulting from Coriolis and spin–rotation interactions may be less in the molecule than in the transition state.

Evaluating $N^\ddagger_{EV}(E-E_0,B_2)$ is a matter of choosing a transition state bend frequency and counting the number of open channels. At threshold ($N^\ddagger = 1$), the experimentally determined density of vibronic states of ~ 0.3 per cm^{-1} yields $k_{uni} \sim 10^{11}$ s^{-1}. This is the same order of magnitude as the experimental rate just above threshold (about a factor of 2 difference). Some of the uncertainty of RRKM calculations (e.g., poor knowledge of the density of states and the necessity to invoke imprecise *ab initio* frequencies for the transition state, or to guess them) has been eliminated. Indeed, we used an experimentally determined density of states (which may well be an underestimate) to infer the threshold rate. So differences between the experimental and calculated rates cannot be casually attributed to ill-defined characteristics of the transition state and the highly excited molecule.

The observed rate can be reconciled with Eq. (1) if one takes $N^\ddagger = 2$ to be the first step in $k_{uni}(E)$, assigning the factor of 2 to the degeneracy of two identical N–O bonds. However, due to molecular symmetry, every rovibronic level has either A_1 or A_2 character in the PI symmetry group. The A_1 species may be viewed as symmetric superpositions of wave functions representing dissociations along each of the bonds, with the A_2 species as antisymmetric ones. Only the A_2 levels are prepared by one-photon laser excitation, so such degeneracy is eliminated. Moreover, the discrepancy between Eq. (1) and the experimen-

tal rates increases slightly if we assume that both the $^2A_2$ and $^2B_1$ surfaces contribute to $\rho(E)$.

It is possible that a discrepancy of a factor of 2 is due to intrinsic inaccuracy of the RRKM formula. Maybe. Finally, we draw attention to the fact that, experimentally, NO$_2$ molecules are excited via the $^2B_2$ electronic state and that the *ab initio* calculations of Jackels and Davidson place the conical intersection between the $^2B_2$ and $^2A_1$ states close to the exit valley leading to the products.[47] It is possible that the IVR process is not complete on the time scale of unimolecular decomposition and that the proximity of the conical intersection to the exit channel facilitates unimolecular decay of optically prepared molecules.

E. How $^2A_1/^2B_2$ mixing affects observed decomposition rates

To discuss the rates quantitatively, it is necessary to take into account the mixed $^2A_1/^2B_2$ electronic character of the ensemble of states excited by the broadband laser pulse. If the zeroth order $^2B_2$ surface is nonreactive at the energies of interest (i.e., correlates with electronically excited products), then only the $^2A_1$ part of the wave function contributes to dissociation. Thus, other things being equal, states having a large percentage of $^2A_1$ character will dissociate faster than states that have a small percentage of $^2A_1$ character. For statistical microcanonical ensembles, the relative amounts of $^2A_1$ and $^2B_2$ character are given by the ratio of the densities of states for the two electronic manifolds $\rho(E,A_1)/\rho(E,B_2)$.

On the other hand, electric dipole excitation is promoted by $^2B_2$ character. Consequently, excited states that have large electric dipole matrix elements with the ground state will tend to dissociate more slowly than those that have small matrix elements. Because of the broad pump laser bandwidth, the observed rates include contributions from many decaying zeroth order states ψ_i of mixed $^2A_1/^2B_2$ character, so they are weighted averages of the rates for individual zeroth order states. The weighting is such that observations are biased toward states that have smaller reaction rates than their "dark" (i.e., primarily $^2A_1$) counterparts. Note that the effect being discussed causes the calculated rates to decrease, thus increasing the difference between the measured and calculated rates. Nonetheless, we deem it important to examine this effect more quantitatively.

For the case of mixed $^2A_1/^2B_2$ electronic character, a zeroth order vibronic state can be written

$$\psi_i = \alpha_i \psi_e(A)\chi_i(A) + \beta_i \psi_e(B)\chi_i(B), \qquad (9)$$

where $\psi_e(A,B)$ and $\chi_i(A,B)$ are normalized electronic and vibrational wave functions for the $^2A_1$ and $^2B_2$ manifolds, respectively, and $|\alpha_i|^2 + |\beta_i|^2 = 1$. Note that $\chi_i(A,B)$ are not vibrational eigenfunctions for the corresponding electronic manifolds, but rather linear combinations of these.

Following the notation of Eq. (9) and using the fact that only the $^2A_1$ part of ψ_i contributes to dissociation, the decay rate is given by

$$k_i = d|\psi_i|^2/dt = |\alpha_i|^2 d|\chi_i(A)|^2/dt, \qquad (10)$$

where $d|\chi_i(A)|^2/dt$ is identified as a rate $k(A)_i$ for the ground electronic PES. In the limit of high densities of states, Eq. (10) yields an expression for the observed rate in terms of of the $^2A_1$ and $^2B_2$ vibrational state densities

$$k_i=|\alpha_i|^2 k(A)_i=\frac{\rho_V(E,A_1)}{\rho_V(E,A_1)+\rho_V(E,B_2)}\, k(A)_i. \quad (11)$$

The density of states ratio is ~ 0.8 at the energies of interest.[67] This is not a large enough effect to warrant concern in the present study. Electric dipole excitation of ground state molecules $\psi_0=\psi_e(A)\chi_0(A)$ to the excited state ψ_i yields an amplitude that is proportional to

$$\langle\psi_i|\mu|\psi_0\rangle|\psi_i\rangle=\beta_i\langle\psi_e(B)\chi_i(B)|\mu|\psi_e(A)\chi_0(A)\rangle|\psi_i\rangle, \quad (12a)$$

$$=\beta_i\langle\psi_e(B)|\mu|\psi_e(A)\rangle\langle\chi_i(B)|\chi_0(A)\rangle|\psi_i\rangle, \quad (12b)$$

$$=\beta_i\mu_e\langle\chi_i(B)|\chi_0(A)\rangle|\psi_i\rangle, \quad (12c)$$

where $\mu_e\equiv\langle\psi_e(B)|\mu|\psi_e(A)\rangle$ and we assume that $\langle\psi_i(A)|\mu|\psi_0\rangle=0$. Thus, the probability of optically preparing ψ_i is proportional to the fractional $^2B_2$ character β_i^2 and to the Franck–Condon factors $|\langle\chi_i(B)|\chi_0(A)\rangle|^2$. For a broadband laser pulse exciting many ψ_i, the observed rate is obtained by averaging over the excitation bandwidth

$$k_{\text{obs}}=\frac{\Sigma_i P_i|\beta_i|^2|\langle\chi_i(B)|\chi_0(A)\rangle|^2(1-|\beta_i|^2)k(A)_i}{\Sigma_i P_i|\beta_i|^2|\langle\chi_i(B)|\chi_0(A)\rangle|^2}; \quad (13)$$

where P_i is the laser intensity at the energy of ψ_i and coherent effects in the excitation and fragmentation processes are neglected. Because of the so-called chaotic nature of nuclear motion at energies near D_0,[68,69] we anticipate that (i) the β_i; (ii) the Franck–Condon factors;[70] and (iii) $k(A)_i$ may all vary significantly from one ψ_i to the next. Furthermore, these quantities are not necessarily correlated. Under certain conditions [e.g., when the $k(A)_i$ values and the Franck–Condon factors are both independent of the index i], Eq. (13) reduces to Eq. (11), but this need not be the case, especially for a small molecule like NO$_2$.

F. Implications about product excitations—the separate statistical ensembles (SSE) method

In the separate statistical ensembles (SSE) method of calculating nascent product vibrational, rotational, and c.m. translational (V,R,T) distributions, product vibrational distributions are obtained by equilibrating $3N-6$ parent degrees of freedom.[31] The precise form assigned to the "transitional modes" (i.e., those evolving from parent vibration to product R,T excitations) may vary from one molecule to the next (e.g., tight vs loose transition states), but the heart of the calculation is to exclude overall parent rotation from the phase space used for calculating product vibrations. Said differently, parent rotational excitation is ineffective at exciting product vibrations, which derive solely from the $3N$-6 parent vibrational degrees of freedom. On the other hand, parent rotation combines with the transitional modes to form product R,T excitations, subject

only to energy and angular momentum constraints. Below the energy threshold for product vibrational excitation, SSE is identical to PST. Above this threshold, SSE predicts that product rotations will appear "colder" than product vibrations—a feature that has been seen in many experiments.[31(a),58]

The SSE method is easy to implement and has been applied to NCNO and CH$_2$CO unimolecular decompositions, where there exist extensive data bases. This has resulted in excellent agreement between experiment and theory.[58] For NO$_2$, with only three vibrational degrees of freedom, the probability of forming NO in $v=1$ is given by

$$P(v=1)=\frac{\rho^{2D}[E^\dagger-E(v=1)]}{\rho^{2D}(E^\dagger)+\rho^{2D}[E^\dagger-E(v=1)]}, \quad (14)$$

where ρ^{2D} is the two-dimensional density of states for the combined bending and reaction coordinate degrees of freedom, and $E(v=1)$ is the energy of NO$(v=1)$; fine structure splittings in NO$(X\ ^2\Pi)$ and O(^3P) are suppressed and it is assumed that NO$(v=2)$ is energetically inaccessible. For the case where the two low frequency transitional modes are treated as unhindered motions, ρ^{2D} is independent of energy and Eq. (14) gives a step function at the $v=1$ threshold with equal probability for $v=0$ and $v=1$. When the $v=2$ channel becomes energetically accessible, the denominator in Eq. (14) acquires the term $\rho^{2D}\{E^\dagger-E(v=2)\}$ and the probabilities for $v=0$, 1, and 2 are each equal to 1/3, etc. for higher v. This "loosest of all possible transition states" assumption worked well for NCNO, where rate measurements confirmed that low frequency transition state vibrations were necessary to reconcile the data. Equation (14) apportions vibrations as per phase space volumes, rather than the fluxes required by transition state theory. This results in vibrationally adiabatic channels; this will be discussed further in a future publication.

The example given above with ρ^{2D} equal to a constant is a limiting case. For NO$_2$, with transition state levels spaced by ~ 100 cm^{-1}, this assumption cannot be made. The observed $k(E)$ structure implies a tighter transition state than for NCNO and CH$_2$CO, and consequently this must be introduced into the SSE formula. With levels for the bend degree of freedom counted directly, Eq. (14) becomes

$$P(v=1)=\frac{\Sigma\rho^{1D}[E^\dagger-E(v=1)]}{\Sigma\rho^{1D}(E^\dagger)+\Sigma\rho^{1D}[E^\dagger-E(v=1)]}, \quad (15)$$

where the summations are over the bending levels and $\rho^{1D}\propto E^{-1/2}$ describes reaction coordinate motion. We do not have enough information to model the bending energy levels, which can be expected to be rotor-like at high energies. However, it is instructive to treat the bend as a low frequency (classical) oscillator. This yields

$$P(v=1)=\frac{[E^\dagger-E(v=1)]^{1/2}}{(E^\dagger)^{1/2}+[E^\dagger-E(v=1)]^{1/2}}. \quad (16)$$

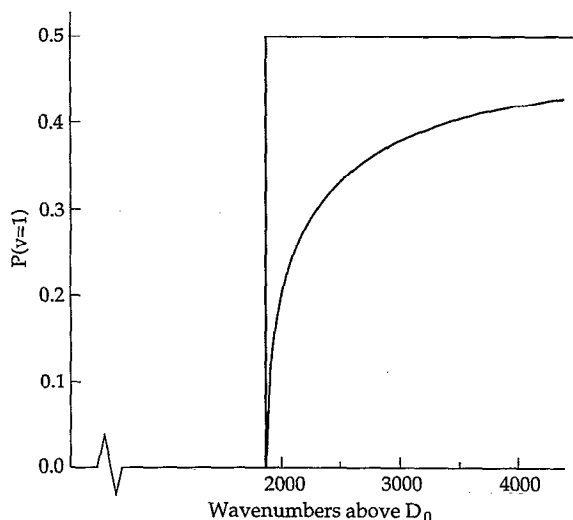At energies where the bend is better represented as a rotor, Eq. (16) underestimates $P(v=1)$, so Eq. (16) should also

FIG. 11. The probability of forming NO(v=1) calculated by using the SSE method. The step function uses a "loosest possible transition state" assumption. The other curve treats the bend as a low frequency oscillator (see the text for details).
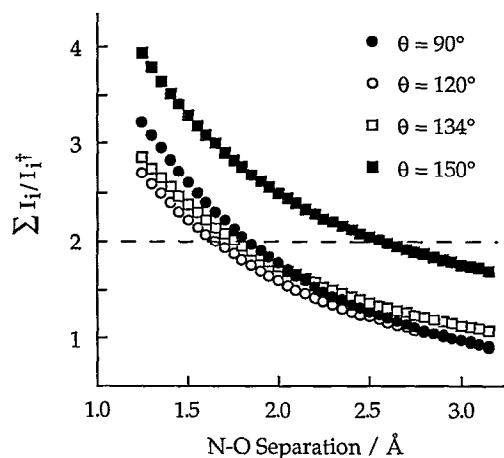

FIG. 12. Relative changes in the NO$_2$ moments of inertia as one of the N–O bonds is stretched, while the other N–O distance is kept equal to its equilibrium value (1.19 Å) (Ref. 65). Different curves correspond to different bond angles, as indicated. θ=120° is the *ab initio* direction of the exit valley (Ref. 47). The dashed line is the experimental result.

be considered a special case. Qualitatively, bending character at the transition state causes $P(v=1)$ to rise rapidly toward the limiting value of 0.5, rather than undergo an abrupt step function. Figure 11 shows the two special cases; reality may lie in between. We note that Eq. (16) is in qualitative agreement with the NO vibrational populations reported recently by Reisler and co-workers[24] as well as variational RRKM calculations[71] (see Table IV).

G. The role of NO$_2$ rotations—transition state ON–O bond length

For a given photolysis wavelength, increasing the amount of NO$_2$ rotational excitation results in an increase in the decomposition rate, in accord with unimolecular decay theories.[1,2] As the ON–O bond stretches, moments of inertia increase, slowing molecular rotation because of angular momentum conservation. The rotational energy E_R is a quadratic function of angular frequency ω, and therefore a reduction in ω is accompanied by a decline in E_R. This lowers the energy needed for dissociation, thereby enhancing the reaction rate. Though the ON–O distance is ultimately increased to infinity, only the energy transferred in the initial stage of bond rupture (i.e., until the transition

TABLE IV. Relative vibrational populations $(v=1)/[(v=0)+(v=1)]$; experimental and RRKM results are from Refs. 24 and 71, respectively. The SSE results use Eq. (11).

Energy above D_0	Experiment	RRKM	SSE
1949	0.28±0.04	0.24	0.16
1998	0.21±0.03	0.27	0.20
2061	0.20±0.03	0.29	0.23
2200	0.42±0.06	0.33	0.28
2700	0.44±0.07	0.38	0.36
3038	0.41±0.06	0.39	0.38

state is reached) influences the rate. These considerations provide an estimate for E_R at the transition state. As shown in Appendix B,

$$\langle E_R^\ddagger \rangle \approx (I_1/I_1^\ddagger + I_2/I_2^\ddagger + I_3/I_3^\ddagger)(kT/2), \qquad (17)$$

where $\langle E_R^\ddagger \rangle$ is the average rotational energy in the transition state; $I_i^\ddagger$ and I_i are the principal moments of inertia at the transition state and equilibrium configurations, respectively. Comparing the experimental rates for expansion cooled and room temperature samples, one finds that for a given photolysis wavelength, the latter correspond to energies that are ~100 cm^{-1} higher than with rotationally cold samples. We attribute this to the above energy transfer mechanism. Thus, Eq. (17) yields

$$(I_1/I_1^\ddagger + I_2/I_2^\ddagger + I_3/I_3^\ddagger) \approx (3kT/2 - 100 \ \text{cm}^{-1})/(kT/2)$$

$$\approx 2 \qquad (18)$$

for T=300 K.

Figure 12 presents $(I_1/I_1^\ddagger + I_2/I_2^\ddagger + I_3/I_3^\ddagger)$ vs ON–O separation for several angles including the 120° *ab initio* transition state of Jackels and Davidson.[47] The N–O equilibrium separation in NO$_2$ (1.19 Å) is close to that of free NO (1.15 Å). In Fig. 12, the bond length of the NO fragment was held at 1.19 Å throughout reaction.[72] Moments of inertia were calculated by diagonalizing the inertia tensor. The dashed line represents the experimental estimate given in Eq. (18). From its intersection with the curve for the 120° *ab initio* bond angle, we obtain a 1.7 Å ON–O distance at the transition state, i.e., ~40% larger than at equilibrium.

V. CONCLUSIONS

Time resolved measurements of NO$_2$ decomposition rates reveal a step-like increase of $k(E)$ for rotationally cold samples. On the other hand, room temperature samples demonstrate a smooth increase of k_{uni} vs photolysis

wavelength. The present results argue for a transition state region in which the NO$_2$ bending frequency has dropped from 758.6 to ~100 cm^{-1}. This degree of tightness in the transition state agrees with earlier values of k_{uni} vs photolysis wavelength determined by Troe and co-workers using room temperature samples,[54] when these results are combined with recent spectroscopic measurements which provide estimates of the density of states near D_0.[22,42,43] Furthermore, this degree of tightness is consistent with a comparison between expansion cooled and room temperature rates, which suggests an ON–O distance of ~1.7 Å in the transition state region.

The present results also have implications regarding product state distributions—e.g., NO vibrational excitation estimated by using the SSE method. Above the NO($v=1$) threshold, the $(v=1)/[(v=0)+(v=1)]$ ratio is expected to rise quickly toward a limiting value of 0.5. This rapid rise is observed experimentally by Reisler and co-workers.[24] Quantum fluctuations may also be reflected in the vibrational populations.[52]

To this day, NO$_2$ remains mysterious, but less so than in the past. A unimolecular decomposition mechanism is now clearly implicated and deviations from more traditional behavior are probably direct manifestations of the $^2A_1/^2B_2$ coupling and the small phase space of this triatom.

Note added in proof. It has very recently come to our attention that the authors of Ref. 22 have measured the NO$_2$ level density in the 5 cm^{-1} interval just below D_0, yielding a value which is an order of magnitude larger than their earlier report, and they have also observed narrow linewidths in yield spectra in the 5 cm^{-1} interval above D_0. This PST-like behavior which is characteristic of reaction threshold cannot be seen in our measurements with their lower resolution. However, tightening of the transition state at higher energies eliminates such PST behavior, as is well known from variational RRKM theory.

ACKNOWLEDGMENTS

APPENDIX A: NEAR THRESHOLD DENSITY OF STATES

To discuss the near threshold density of optically accessible states, we start from selection rules. The NO$_2$ permutation–inversion (PI) group is isomorphous to the C_{2v} point group,[73] so the notations of the latter are used. Since PI symmetry originates from exchange of identical nuclei, it describes the exact Hamiltonian and characterizes eigenstates of the whole system including reactants and products. Due to the zero nuclear spin of ^{16}O, every rovibronic state of bound or dissociating NO$_2$ is described by A_1 or A_2 symmetry species; B_1 and B_2 are prohibited by nuclear spin statistics. The following analysis takes into account that only the lowest NO$_2$ states are populated in

the jet, i.e., $v_i'' = 0$, even N'', and $K''=0$, where v_i'' are vibrational quantum numbers, N'' is the rotational angular momentum (which only takes on even values for $K''=0$), and K'' is the projection of N'' onto the axis of lowest moment of inertia. These states are characterized by totally symmetric A_1 species. The ground state rovibronic eigenfunction may be approximated as a product of electronic, vibrational, and rotational A_1 functions $\Psi_{E''V''R''} = \Psi_{E''}\Psi_{V''}\Psi_{R''}$.

Selection rules for an electric dipole transition from A_1 are[72] (i) $A_2\leftarrow A_1$ for rovibronic transitions; (ii) $A_1\leftarrow A_1$ for vibrational transitions for the $^2B_2\leftarrow ^2A_1$ electronic system (which carries all of the transition moment); (iii) When electronic and vibrational motions are not separable, but the combination is separable from molecular rotation, the vibronic selection rules are $B_2\leftarrow A_1$, and for the accompanying rotational transitions, we have $B_1\leftarrow A_1$, $K'=K''$, and $N'=N''\pm 1$. In summary, A_2 rovibronic, B_2 vibronic, A_1 vibrational, and B_1 rotational states are accessible by a one quantum electronic transition from the A_1-symmetry states populated in the jet. However, all excited state symmetries and the corresponding selection rules, except for the rovibronic species and for the total angular momentum including spin $J'=J''\pm 1$, are approximate and may be broken by various intramolecular interactions as discussed below.

With the approximation $\Psi_{E'V'R'} = \Psi_{E'(2B2)}\Psi_{V'}(A_1)\Psi_{N'K'}$, the density of optically prepared states having rotational angular momentum N' is comprised of $\Psi_{V'}(A_1)$ vibrational states on the $^2B_2$ surface; it is hereafter referred to as $\rho_{2B_2}(A_1)$. However, the Born–Oppenheimer approximation does not hold for NO$_2$ in the threshold region due to the $^2A_1/^2B_2$ conical intersection. Mixing is so strong that attempts to assign eigenstates to either of the two surfaces fail even at energies ~10 000 cm^{-1}, and vibronic chaos exists above ~16 000 cm^{-1}.[43] Consequently, $\Psi_{E'}(^2A_1)\Psi_{V'}(B_2)$ vibronic states borrow dipole moment from $\Psi_{E'}(^2B_2)\Psi_{V'}(A_1)$ states which are characterized by the same B_2 vibronic symmetry. Thus, all B_2 vibronic states with combined density $\rho_{EV}(B_2) = \rho_{2A_1}(B_2) + \rho_{2B_2}(A_1)$ are optically accessible.

Fortunately, experimentally based estimates of vibronic state densities can be obtained near D_0. For example, Delon *et al.* examined NO$_2$ spectra in detail in the region 16 500–18 500 cm^{-1}, reporting 159 B_2 vibronic levels of the $^2A_1/^2B_2$ mixed states.[43] Extrapolating from the levels observed below 10 000 cm^{-1},[42] they deduced that there are 210 levels in the 16 500–18 500 cm^{-1} interval. Taking $\rho_{EV}(B_2)\sim0.1$ per cm^{-1} at 17 500 cm^{-1} and extrapolating to D_0 by assuming that the density increases as $(E+E_{00})^2$,[74] where $E_{00}=1844$ cm^{-1} is the NO$_2$ zero point vibrational energy, yields $\rho_{EV}(B_2)\sim0.2$ per cm^{-1} near D_0.

A more precise evaluation of the near-threshold density of rovibronic states may be obtained by examining the LIF spectra recently reported for expansion cooled samples, i.e., 1 K, with 98% of the NO$_2$ molecules on the lowest rotational level. Under these conditions, Miyawaki

et al. observe more than 60 transitions in a 25 cm^{-1} region immediately below D_0.[22] Since $J=1/2$ for the lowest rotational level, a one-photon transition takes molecules to $J=1/2$ and 3/2 levels, each contributing to the observed density of spectral lines. Other groups[20] have also reported highly structured spectra below D_0 which are in general agreement with the Miyawaki *et al.* results. Above D_0, lifetime broadening results in overlap of zeroth order levels, making it impractical to recover level densities from absorption spectra.

The results of Miyawaki *et al.* indicate that the observed level density near D_0 is higher than that obtained by extrapolating the vibronic level density from 10 000 cm^{-1}. The difference is most likely due to spin–rotation and Coriolis couplings. Coriolis interaction mixes all rotational states of the same symmetry for a given rotational angular momentum N'. Such mixing destroys the K' quantum number and increases the density of optically accessible states by a factor of $(N'+1)/2$ or $N'/2$, depending on whether N' is odd or even. In turn, N' is not a good quantum number at energies above about 20 000 cm^{-1} because of spin–rotation interactions.[40] For total angular momentum $J'=N'\pm1/2$, N' takes on both even and odd numbers. As a result of both K and N breakdowns, the number of spectral lines increases by a factor of $(2J'+1)/2$. Finally, Coriolis interaction mixes B_2 and A_1 vibronic species of the same rovibronic symmetry, which doubles the number of optically accessible states of given angular momentum and symmetry $\rho(J',A_2)=(2J'+1)\rho_{EV}(B_2)$. Taking into account the extremely low NO$_2$ rotational temperature in the experiments by Miyawaki *et al.*,[22] we find that only those transitions that originate from the ground rotational level are present in their spectra. Therefore, their experimental density of lines corresponds to the combined density of A_2 symmetry states for $J'=1/2$ and 3/2, i.e., $\rho(1/2,A_2)+\rho(3/2,A_2)=2\rho_{EV}(B_2)+4\rho_{EV}(B_2)=6\rho_{EV}(B_2)$. As a result, we obtain $\rho_{EV}(B_2)\approx0.3$ levels/cm^{-1} which is close to the above estimates based on the results by Delon and Jost.[42,43] Since our estimates are based on visual inspection of published spectra which are recorded with limited resolution and S/N, there may be additional levels. Therefore, we write $\rho_{EV}(B_2)\gtrsim0.3$ levels/cm^{-1}.

APPENDIX B: ROTATIONAL ENERGY CHANGE IN DISSOCIATING NO$_2$

As a first step in calculating the rotational energy change in dissociating NO$_2$, we note that the I_3 moment of inertia is considerably smaller than I_1 or I_2.[75] This inequality is retained during bond rupture I_1 and I_2 increase, while I_3 remains approximately constant. For a planar molecule, $I_1=I_2+I_3$, giving $I_1\approx I_2$, i.e., NO$_2$ may be treated as a near symmetric top, which facilitates analysis. For a rotating symmetric top ($I_1=I_2=I$), one has[76]

$$d(I\omega_1)/dt=\omega_2\omega_3(I-I_3), \quad d(I\omega_2)/dt=\omega_1\omega_3(I_3-I),$$

$$d(I_3\omega_3)/dt=0, \tag{B1}$$

where rotational frequencies ω_i are given with respect to instantaneous positions of the principal axis. The projection $I_3\omega_3$ of the angular momentum onto the third symmetry axis is conserved in the course of geometrical transformations as long as the symmetric top approximation remains valid. Moreover, the sum of the squares of the two other components $(I\omega_1)^2+(I\omega_2)^2$ is also conserved. Taking this into account,

$$E_{rot}^\dagger\approx I^\dagger(\omega_1^{\dagger2}+\omega_2^{\dagger2})/2+I_3^\dagger\omega_3^{\dagger2}/2=(I/I^\dagger)E_{1+2}+(I_3/I_3^\dagger)E_3, \tag{B2}$$

where E_{1+2} and E_3 are the initial energies in the first two and third rotational degrees of freedom, respectively. Averaging Eq. (A2) over a room temperature Boltzmann distribution yields

$$\langle E_{rot}^\dagger\rangle\approx(kT/2)(2I/I^\dagger+I_3/I_3^\dagger). \tag{B3}$$

[1] P. J. Robinson and K. A. Holbrook, *Unimolecular Reactions* (Wiley, London, 1972).
[2] W. Forst, *Theory of Unimolecular Reactions* (Academic, New York, 1973).
[3] P. Pechukas and J. C. Light, J. Chem. Phys. **42**, 3281 (1965).
[4] C. E. Klots, J. Phys. Chem. **75**, 1526 (1971).
[5] M. Quack and J. Troe, Ber. Bunsenges. Phys. Chem. **78**, 240 (1974).
[6] M. Quack and J. Troe, Ber. Bunsenges. Phys. Chem. **79**, 170 (1975).
[7] M. Quack and J. Troe, Ber. Bunsenges. Phys. Chem. **79**, 469 (1975).
[8] H. Reisler and C. Wittig, Annu. Rev. Phys. Chem. **37**, 307 (1986), and references therein.
[9] *Molecular Photodissociation Dynamics*, edited by M. N. R. Ashfold and J. E. Baggot (Royal Society of Chemistry, Bristol, 1987), and references therein.
[10] *Bimolecular Collisions*, edited by M. N. R. Ashfold and J. E. Baggot (Royal Society of Chemistry, Bridport, 1989), and references therein.
[11] C. X. W. Qian, M. Noble, I. Nadler, H. Reisler, and C. Wittig, J. Chem. Phys. **83**, 5573 (1985).
[12] D. J. Nesbitt, H. Petek, M. F. Foltz, S. V. Filseth, D. J. Bamford, and C. B. Moore, J. Chem. Phys. **83**, 223 (1985).
[13] T. M. Ticich, T. R. Rizzo, H. R. Dübal, and F. F. Crim, J. Chem. Phys. **84**, 1508 (1986).
[14] A. Sinha, R. L. Vander Wal, and F. F. Crim, J. Chem. Phys. **92**, 401 (1990).
[15] S. K. Kim, Y. S. Choi, C. D. Pibel, Q.-K. Zheng, and C. B. Moore, J. Chem. Phys. **94**, 1954 (1991).
[16] I.-C. Chen, W. H. Green, and C. B. Moore, J. Chem. Phys. **89**, 314 (1988).
[17] W. H. Green, A. J. Mahoney, Qi-Ke Zheng, and C. B. Moore, J. Chem. Phys. **94**, 1961 (1991).
[18] H. Zacharias, M. Geilhaupt, K. Meier, and K. H. Welge, J. Chem. Phys. **74**, 218 (1981).
[19] H. Zacharias, K. Meier, and K. H. Welge, in *Energy Storage and Redistribution in Molecules*, edited by J. Hinze (Plenum, New York, 1983), p. 107.
[20] U. Robra, H. Zacharias, and K. H. Welge, Z. Phys. D **16**, 175 (1990).
[21] J. Miyawaki, T. Tsuchizawa, K. Yamanouchi, and S. Tsuchiya, Chem. Phys. Lett. **165**, 168 (1990).
[22] J. Miyawaki, K. Yamanouchi, and S. Tsuchiya, Chem. Phys. Lett. **180**, 287 (1991).
[23] J. McFarlane, J. C. Polanyi, and J. G. Shapter, J. Photochem. Photobiol. A **58**, 139 (1991).
[24] D. C. Robie, M. Hunter, J. L Bates, and H. Reisler, Chem. Phys. Lett. **193**, 413 (1992).
[25] W. Polik, D. R. Guyer, and C. B. Moore, J. Chem. Phys. **92**, 3453 (1990).
[26] L. R. Khundar, J. L. Knee, and A. H. Zewail, J. Chem. Phys. **87**, 77 (1987).
[27] E. D. Potter, M. Gruebele, L. R. Khundar, and A. H. Zewail, Chem. Phys. Lett. **164**, 463 (1989).
[28] R. A. Marcus, Chem. Phys. Lett. **144**, 208 (1988).
[29] S. J. Klippenstein and R. A. Marcus, J. Phys. Chem. **92**, 3105 (1988).

[30] S. J. Klippenstein and R. A. Marcus, J. Phys. Chem. 92, 5412 (1988).

[31] (a) C. Wittig, I. Nadler, H. Reisler, J. Catanzarite, and G. Radhakrishnan, J. Chem. Phys. 83, 5581 (1985); (b) J. Troe, ibid. 85, 1708 (1986); (c) C. Wittig, I. Nadler, H. Reisler, J. Catanzarite, and G. Radhakrishnan, ibid. 85, 1710 (1986).

[32] R. E. Smalley, L. Wharton, and D. H. Levy, J. Chem. Phys. 63, 4977 (1975).

[33] D. Hsu, D. L. Monts, and R. N. Zare, Spectral Atlas of Nitrogen Dioxide 5530 to 6480 Å (Academic, New York, 1978).

[34] C. H. Chen, D. W. Clark, M. G. Payne, and S. D. Kramer, Opt. Commun. 32, 391 (1980).

[35] H. Köppel, W. Domcke, and L. S. Cederbaum, Adv. Chem. Phys. 57, 59 (1984), and references therein.

[36] E. A. Rohlfing and J. J. Valentini, J. Chem. Phys. 83, 521 (1985).

[37] J. L. Hardwick, J. Mol. Spectrosc. 109, 85 (1985).

[38] E. Haller, H. Köppel, and L. S. Cederbaum, J. Mol. Spectrosc. 111, 377 (1985).

[39] H. Nagai, K. Shibuya, and K. Obi, J. Mol. Spectrosc. 126, 427 (1987).

[40] K. Shibuya, T. Kusumoto, H. Nagai, and K. Obi, Chem. Phys. Lett. 152, 129 (1988).

[41] S. Hiraoka, K. Shibuya, and K. Obi, J. Chem. Phys. 93, 7656 (1990).

[42] A. Delon and R. Jost, J. Chem. Phys. 95, 5686 (1991).

[43] A. Delon, R. Jost, and M. Lombardi, J. Chem. Phys. 95, 5700 (1991).

[44] L. Burnelle, A. M. May, and R. A. Gangi, J. Chem. Phys. 49, 561 (1968).

[45] R. A. Gangi and L. Burnelle, J. Chem. Phys. 55, 851 (1971).

[46] G. D. Gillispie, A. V. Khan, A. C. Wahl, R. P. Hosteny, and M. Krauss, J. Chem. Phys. 63, 3425 (1975).

[47] C. F. Jackels and E. R. Davidson, J. Chem. Phys. 64, 2908 (1976).

[48] C. F. Jackels and E. R. Davidson, J. Chem. Phys. 65, 2941 (1976).

[49] G. E. Busch and K. R. Wilson, J. Chem. Phys. 56, 3626 (1972); 56, 3638 (1972).

[50] M. Kawasaki, H. Sato, A. Fukuroda, T. Kikuchi, S. Kobayashi, and T. Arikawa, J. Chem. Phys. 86, 4431 (1987).

[51] D. C. Robie, M. Hunter, J. L. Bates, and H. Reisler, Chem. Phys. Lett. 193, 413 (1992).

[52] S. A. Reid, D. C. Robie, M. Hunter, and H. Reisler (unpublished).

[53] T. Ericson, Phys. Rev. Lett. 5, 430 (1960).

[54] H. Gaedtke, H. Hippler, and J. Troe, Chem. Phys. Lett. 16, 177 (1972).

[55] D. M. Wardlaw and R. A. Marcus, J. Chem. Phys. 83, 3462 (1985).

[56] B. M. Toselli and J. R. Barker, J. Chem. Phys. 91, 2239 (1989).

[57] E. R. Lovejoy, S. K. Kim, and G. B. Moore, Science 256, 1541 (1992).

[58] H. Reisler and C. Wittig, in Advances in Kinetics and Dynamics, edited by J. R. Barker (JAI, Greenwich, 1992), Vol. 1.

[59] Preliminary observations reported in G. A. Brucker, S. I. Ionov, Y. Chen, and C. Wittig, Chem. Phys. Lett. 194, 301 (1992).

[60] E. Pollak, J. Chem. Phys. 74, 5586 (1981).

[61] W. H. Miller, R. Hernandez, C. B. Moore, and W. F. Polik, J. Chem. Phys. 93, 5657 (1990).

[62] S. J. Klippenstein and R. A. Marcus, J. Chem. Phys. 91, 2280 (1989).

[63] S. J. Klippenstein, L. R. Khundar, A. H. Zewail, and R. A. Marcus, J. Chem. Phys. 89, 4761 (1988).

[64] S. Bashkin and J. O. Stoner, Jr., Atomic Energy Levels and Grothrian Diagrams 1 (North Holland, New York, 1975).

[65] G. Herzberg, Molecular Spectra and Molecular Structure (Van Nostrand–Reinhold, New York, 1950), Vol. 1.

[66] O. K. Rice and H. Gershinowitz, J. Chem. Phys. 2, 853 (1934).

[67] I. W. M. Smith, Int. J. Chem. Kinet. 16, 423 (1984).

[68] See T. A. Brody, J. Flores, J. B. French, P. A. Mello, A. Pandey, and S. S. M. Wong, Rev. Mod. Phys. 53, 385 (1981), and references therein.

[69] C. E. Porter and R. G. Thomas, Phys. Rev. 15, 483 (1956).

[70] G. D. Gillispie and A. U. Khan, J. Phys. Chem. 65, 1624 (1976).

[71] S. J. Klippenstein and T. Radivoyevitch, J. Chem. Phys. (to be published).

[72] G. R. Bird, J. C. Baird, A. W. Jache, J. A. Hodgeson, R. F. Curl, Jr., A. C. Kunkle, J. W. Bransford, J. Rastrup-Andersen, and J. Rosenthal, J. Chem. Phys. 40, 3378 (1964).

[73] D. Papoušek and M. R. Aliev, Molecular Vibrational–Rotational Spectra (Elsevier, Amsterdam, 1982).

[74] R. A. Marcus and O. K. Rice, J. Phys. Colloid. Chem. 55, 894 (1951).

[75] G. Herzberg, Molecular Spectra and Molecular Structure (Van Nostrand–Reinhold, New York, 1966), Vol. 3.

[76] H. Goldstein, Classical Mechanics, 2nd ed. (Addison–Wesley, Menlo Park, CA, 1980).